Inorg. Chem. **2007**, *46*, 2824–2835

Synthesis, Characterization, and Photochromic Properties of Hybrid Organic–Inorganic Materials Based on Molybdate, DABCO, and Piperazine

Violaine Coué, Rémi Dessapt, Martine Bujoli-Doeuff, Michel Evain, and Stéphane Jobic*

Institut des Matériaux Jean ROUXEL, UMR 6502 CNRS, Laboratoire de Chimie des Solides, Université de Nantes, 2 rue de la Houssinière, BP 32229, 44322 Nantes Cedex 3, France

Received November 13, 2006

Prompted by our interest in new photochromic organic–inorganic hybrid materials, the reactivity of $[Mo_7O_{24}]^{6-}$ toward a structure-directing reagent diamine such as 1,4-diazabicyclo[2.2.2]octane (DABCO) and piperazine (pipz) has been investigated, and three new molybdenum(VI)-containing compounds, namely, $(H_2DABCO)_3[Mo_7O_{24}]\cdot 4H_2O$ (**1**), $(H_2DABCO)[Mo_3O_{10}]\cdot H_2O$ (**2**), and $(H_2DABCO)_2(NH_4)_2[Mo_8O_{27}]\cdot 4H_2O$ (**3**), have been synthesized and characterized. New synthetic routes to achieve the known compounds $(H_2DABCO)_2(H_2pipz)[Mo_8O_{27}]$ (**4**), $(H_2pipz)_3[Mo_8O_{27}]$ (**5**), and $(H_2DABCO)_2[Mo_8O_{26}]\cdot 4H_2O$ (**6**) are also reported. All of these compounds contain different poly(oxomolybdate) clusters, i.e., discrete $[Mo_7O_{24}]^{6-}$ blocks in **1**, infinite polymeric chains $^1/_\infty[Mo_3O_{10}]^{2-}$ in **2**, $^1/_\infty[Mo_8O_{27}]^{6-}$ in **3**–**5**, and $^1/_\infty[Mo_8O_{26}]^{4-}$ in **6**, associated in a tridimensional assembly by hydrogen bonds with H_2DABCO^{2+} and/or H_2pipz^{2+} cations. Interconversion pathways and chemical factors affecting the stabilization of the different species are highlighted and discussed. At the opposite of **6**, compounds **1**–**5** show photochromic behavior under UV excitation. Namely, compounds **1**–**5** shift from white or pale yellow to pale pink, reddish brown, or purple under UV illumination depending on the chemical nature of the mineral framework, with the kinetics of the color change being dictated by the nature of the organic component and by the organic–inorganic interface.

Introduction

Investigations into X-chromic materials, i.e., compounds that undergo a well-observable color change upon the application of an external stimulus, have been extensive over the past decade. Beyond them, photochromic materials that are able to modify their coloration with light have found uses in a wide variety of applications such as ophthalmic lenses, printing, cosmetics, switches and sensors, optical data storage, etc. While pure organic[1,2] and inorganic photochromic materials[3−5] have been known for a long time, much attention has been dedicated to the development of new hybrid organic−inorganic materials with photochromic properties in the past few years.

Major photochromic hybrid materials are obtained using the sol−gel process. Namely, these compounds consist of photochromic spiromolecules, such as spiropyrans or spirooxazines, embedded into mineral sol−gel glasses. The photochromism is due to photocleavage of C−O bonds of the colorless spiro fragments under UV irradiation to form a colored open merocyanine structure. The photochromism response (i.e., the kinetics of the color change, the excitation energy, the stability of the photoinduced state, and the fading rate) and the cyclability depend strongly on the dye−host interactions.[6,7] However, because the sol−gel hybrid-derived compounds are generally amorphous, these interactions are not well identified and knowledge of the structure−property relationships is limited.

Hybrid organic−inorganic materials based on polyoxomolybdate (Mo-POM) and organoammonium cations represent also a second class of potentially photochromic materials.[8] In such compounds, the structurally well-defined

* To whom correspondence should be addressed. E-mail: stephane.jobic@cnrs-imn.fr. Tel: +33 2 40 37 39 17. Fax: +33 2 40 37 39 95.

(1) Berkovic, G.; Krongaus, V.; Weiss, V. *Chem. Rev.* **2000**, *100*, 1741−1753.
(2) Irie, M. *Chem. Rev.* **2000**, *100*, 1685−1716.
(3) He, T.; Yao, J. *J. Photochem. Photobiol. C* **2003**, *4*, 125−143.
(4) Nishio, S.; Kakihana, M. *Chem. Mater.* **2002**, *14*, 3730−3733.
(5) Huang, M.-H.; Xia, J.-Y.; Xi, Y.-M.; Ding, C.-X. *J. Eur. Ceram. Soc.* **1997**, *17*, 1761−1765.
(6) Schaudel, B.; Guermeur, C.; Sanchez, C.; Nakatani, K.; Delaire, J. A. *J. Mater. Chem.* **1997**, *7*, 61−65.
(7) Lafuma, A.; Chodorowski-Kimmes, S.; Quinn, F. X.; Sanchez, C. *Eur. J. Inorg. Chem.* **2003**, 331−338.

10.1021/ic0621502 CCC: $37.00
Published on Web 02/27/2007

$Mo_xO_y^{n-}$ building blocks are connected to organic fragments and, sometimes, to solvent molecules via weak interactions (e.g., van der Waals, static, or hydrogen bonds). These compounds have a higher degree of organization than aforementioned materials, which allows a better characterization of the interactions between both organic and inorganic components. The topological diversity of both organoammonium cations and Mo-POM blocks can be used in numerous self-assembling processes, which may trigger the design of a large range of original hybrid frameworks with tunable dimensionality.[9−11] However, most syntheses involve oxolation−condensation reaction types in which the organic counterpart not only acts as a charge-compensating counterpart but often directs the polymerization of the inorganic component and dictates the topology of the final supramolecular assembly.[12] One of the major, remaining questions to address about control of the design of new hybrid materials consists of an understanding of the directing role of organoammonium cations on the structure of the mineral building blocks.

In the course of new organic−inorganic hybrid materials with tunable optical properties, our study attempts to answer two questions: (i) Is it possible to define specific synthesis parameters that allow one to isolate selectively various Mo-POM blocks independent of the nature of the organoammonium part? (ii) Is it possible to obtain a better understanding of the synergetic effect of both organic and inorganic components on the photochromic properties in such hybrid materials? To this aim, we have embarked on the elucidation of the reactivity of molybdate clusters toward amines[13,14] such as 1,8-diazabicyclo[5.4.0]undec-7-ene (DBU), 1,4-diazabicyclo-[2.2.2]octane (DABCO), and piperazine (pipz). This paper focuses principally on a systematic study of the DABCO/$[Mo_7O_{24}]^{6-}$ system in an aqueous medium. We report the synthesis and characterization of six hybrid organic−inorganic compounds built upon four different Mo-POM blocks. The influence of many parameters such as the pH, DABCO/$[Mo_7O_{24}]^{6-}$ ratio, and temperature on the stability of each molybdate block is systematically discussed. The optical properties of the materials are given, and the photochromism of compounds **1**−**5** is argued on the basis of the analysis of different parameters such as both the nature of the inorganic and organic components and the hydrogen bond subnetworks.

Experimental Section

Chemicals. 1,4-Diazabicyclo[2.2.2]octane ($N_2C_6H_{12}$, DABCO), piperazine ($N_2C_4H_{10}$, pipz), MoO_3, and $(NH_4)_6[Mo_7O_{24}]\cdot 4H_2O$ were purchased from Aldrich Chemical Co. All reagents were used without further purification. The purity of all of the prepared, powdered materials was systematically checked by X-ray diffraction, IR measurements, and elemental chemical analyses.

$(H_2DABCO)_3[Mo_7O_{24}]\cdot 4H_2O$ (1). $(NH_4)_6[Mo_7O_{24}]\cdot 4H_2O$ (1.235 g, 1 mmol) was dissolved in 15 mL of water. After the addition of DABCO (0.336 g, 3 mmol), the pH was adjusted to 4.5 with 1 M HCl. The mixture was stirred at room temperature for 3 h and filtered to isolate a white solid of **1**. The powder was washed with H_2O, EtOH, and Et_2O (yield: 93%). Colorless needles of **1** suitable for X-ray structure analysis were obtained by slow evaporation of 30 mL of a water solution containing $(NH_4)_6[Mo_7O_{24}]\cdot 4H_2O$ (0.618 g, 0.5 mmol) and DABCO (0.336 g, 3 mmol) at pH 6, i.e., a pH high enough to favor the crystal growth and to slow down precipitation. Experiments could be reproduced in a large excess of DABCO (namely, with a DABCO to $(NH_4)_6[Mo_7O_{24}]\cdot 4H_2O$ ratio of 6, for instance) and lead to **1** in high yield. Anal. Calcd for $C_{18}H_{50}O_{28}N_6Mo_7$: C, 14.70; H, 3.43; N, 5.71; Mo, 45.68. Found: C, 14.65; H, 3.40; N, 5.65; Mo, 44.32. FT−IR (cm^{-1}): H_2O, 1646 (w); H_2DABCO^{2+} cations, 1473 (m), 1389 (m), 1321 (w), 1279 (w), 1055 (m), 969 (m), 601 (m); ν(Mo═O) 930 (m), 833 (s), 873 (s), 838 (m), 821 (s); ν(Mo−O−Mo) 713 (w), 638 (m), 564 (m), 538 (m), 450 (m), 416 (m). From differential scanning calorimetry/thermogravimetric analysis (DSC/TGA) measurements, **1** is stable up to ∼75 °C.

$(H_2DABCO)[Mo_3O_{10}]\cdot H_2O$ (2). $(NH_4)_6[Mo_7O_{24}]\cdot 4H_2O$ (1.235 g, 1 mmol) was dissolved in 15 mL of water. After the addition of DABCO (0.262 g, 2.33 mmol), the pH was adjusted to 4 with 1 M HCl. The mixture was stirred at room temperature for a few minutes and sealed in a 30-mL Teflon-lined autoclave (130 °C, 4 days, autogenous pressure). The slurry was filtered to isolate for the first time a white solid of **2**. The powder was washed with H_2O, EtOH, and Et_2O (yield: 80%). Unfortunately, following this chemical route, the crystal size turned out to be improper for a single-crystal structure determination. Then, a worthwhile endeavor consisting of the addition of DABCO (0.196 g, 1.75 mmol) to MoO_3 (0.720 g, 5 mmol) in 15 mL of water led to colorless needles of **2** suitable for X-ray structure analysis, with the mixture being stirred at room temperature for a few minutes and sealed in a 30-mL Teflon-lined autoclave (130 °C, 4 days, autogenous pressure). Anal. Calcd for $C_6H_{16}O_{11}N_2Mo_3$: C, 12.42; H, 2.78; N, 4.83; Mo, 49.62. Found: C, 12.55; H, 2.76; N, 4.78; Mo, 48.64. FT−IR (cm^{-1}): H_2O, 1615 (w); H_2DABCO^{2+} cations, 1481 (m), 1394 (m), 1328 (m), 1273 (m), 1244 (w), 1168 (w), 1064 (m), 998 (w), 970 (w), 602 (m); ν(Mo═O, Mo−O−Mo) 931 (m), 908 (s), 881 (s), 844 (m), 807 (w), 762 (w), 659 (m), 643 (s), 626 (s), 470 (m), 423 (w), 409 (w). From DSC/TGA measurements, **2** is stable up to ∼100 °C.

(a) Synthesis of 2 from 1. A slurry of **1** (736 mg, 0.5 mmol) in 15 mL of water (pH 4) was stirred at room temperature for a few minutes and sealed in a 30-mL Teflon-lined autoclave (130 °C, 4 days, autogenous pressure). The resulting white microcrystalline powder of **2** was filtered off and washed with H_2O, EtOH, and Et_2O (yield: 92%).

(b) Synthesis of 2 from 3. DABCO (37 mg, 0.33 mmol) was added to a slurry of **3** (720 mg, 0.47 mmol) in 15 mL of water, and the pH was adjusted to 4 with 1 M HCl. The mixture was stirred at room temperature for a few minutes and sealed in a 30-mL Teflon-lined autoclave (130 °C, 4 days, autogenous pressure). The resulting white microcrystalline powder of **2** was filtered off and washed with H_2O, EtOH, and Et_2O (yield: 95%).

(c) Synthesis of 2 from 6. DABCO (37 mg, 0.33 mmol) was added to a slurry of **6** (742 mg, 0.5 mmol) in 15 mL of water. The mixture was stirred at room temperature for a few minutes and sealed in a 30-mL Teflon-lined autoclave (130 °C, 4 days,

(8) He, T.; Yao, J. *Prog. Mater. Sci.* **2006**, *51*, 810−879.
(9) Roman, P.; San Jose, A.; Luque, A.; Gutierrez-Zorrilla, J. M. *Acta Crystallogr.* **1994**, *C50*, 1189−1191.
(10) Upreti, S.; Ramanan, A. *Inorg. Chim. Acta* **2005**, *358*, 1241−1246.
(11) Zapf, P. J.; Haushalter, R. C.; Zubieta, J. *Chem. Commun*. **1997**, 321−322.
(12) Hagrman, P. J.; Hagrman, D.; Zubieta, J. *Angew. Chem., Int. Ed.* **1999**, *38*, 2638−2684.
(13) Coué, V.; Dessapt, R.; Bujoli-Doeuff, M.; Evain, M.; Jobic, S. *J. Solid State Chem.* **2006**, *179*, 3601−3613.
(14) Evain, M.; Petricek, V.; Coué, V.; Dessapt, R.; Bujoli-Doeuff, M.; Jobic, S. *Acta Crystallogr.* **2006**, *B62*, 790−797.

autogenous pressure). The resulting white microcrystalline powder of **2** was filtered off and washed with H_2O, EtOH, and Et_2O (yield: 90%).

$(H_2DABCO)_2(NH_4)_2[Mo_8O_{27}]\cdot 4H_2O$ (3). $(NH_4)_6[Mo_7O_{24}]\cdot 4H_2O$ (1.235 g, 1 mmol) was dissolved in 15 mL of water. After the addition of DABCO (0.196 g, 1.75 mmol), the pH was adjusted to 4 with 1 M HCl. The mixture was stirred at room temperature for a few minutes and filtered to isolate a pale-yellow solid of **3**. The powder was washed with H_2O, EtOH, and Et_2O (yield: 94%). Anal. Calcd for $C_{12}H_{44}O_{31}N_6Mo_8$: C, 9.38; H, 2.88; N, 5.47; Mo, 49.97. Found: C, 9.34; H, 2.70; N, 5.28; Mo, 49.16. FT−IR (cm^{-1}): H_2O, 1627 (m); H_2DABCO^{2+} cations, 1475 (w), 1320 (w), 1155 (w), 1158 (m), 600 (w); NH_4^+ cations, 1402 (s); ν(Mo═O, Mo−O−Mo) 941 (m), 926 (m), 909 (w), 869 (vs), 837 (s), 769 (m), 693 (m), 645 (m), 558 (m), 533 (m), 500 (m), 474 (m), 441 (w). From DSC/TGA measurements, **3** is stable up to ∼50 °C.

$(H_2DABCO)_2(H_2pipz)[Mo_8O_{27}]$ (4). $(NH_4)_6[Mo_7O_{24}]\cdot 4H_2O$ (1.235 g, 1 mmol) was dissolved in 15 mL of water. After the addition of DABCO (0.196 g, 1.75 mmol) and pipz (0.075 g, 0.875 mmol), the pH was adjusted to 4 with 1 M HCl. The mixture was stirred at room temperature for a few minutes and filtered to isolate a pure, yellowish-white solid of **4**. The powder was washed with H_2O, EtOH, and Et_2O (yield: 91%). Colorless crystals of **4** suitable for X-ray structure analyses have been obtained hydrothermally from an aqueous solution of ammonium heptamolybdate and DABCO only in the ratio of 1:6 (10 days, 160 °C). The formation of H_2pipz^{2+} cations results from the thermal degradation of DABCO. FT−IR (cm^{-1}): H_2DABCO^{2+}, H_2pipz^{2+} cations, 1561 (w), 1470 (w), 1453 (w), 1419 (w), 1394 (w), 1323 (w), 1209 (sh), 1155 (sh), 1086 (sh), 1057 (m), 1012 (sh), 603 (w); ν(Mo═O, Mo−O−Mo) 932 (s), 875 (vs), 865 (vs), 839 (s), 774 (s), 701 (s), 648 (m), 577 (m), 553 (m), 536 (m), 507 (m), 474 (m), 438 (w). From DSC/TGA measurements, **4** is stable up to ∼250 °C.

$(H_2pipz)_3[Mo_8O_{27}]$ (5). $(NH_4)_6[Mo_7O_{24}]\cdot 4H_2O$ (1.235 g, 1 mmol) was dissolved in 15 mL of water. After the addition of pipz (0.228 g, 2.625 mmol), the pH was adjusted to 4 with 1 M HCl. The mixture was stirred at room temperature for a few minutes and filtered to isolate a pure, yellowish-white solid of **5**. The powder was washed with H_2O, EtOH, and Et_2O (yield: 95%). Anal. Calcd for $C_{12}H_{36}O_{27}N_6Mo_8$: C, 9.84; H, 2.48; N, 5.74; Mo, 52.43. Found: C, 9.70; H, 2.45; N, 5.83; Mo, 51.42. FT−IR (cm^{-1}): H_2pipz^{2+} cations, 1622 (w), 1603 (m), 1564 (m), 1482 (w), 1455 (m), 1424 (m), 1412 (m), 1391 (w), 1317 (w), 1212 (w), 1203 (sh), 1166 (sh), 1084 (w), 1069 (w), 1009 (w); ν(Mo═O, Mo−O−Mo) 933 (s), 900 (s), 896 (m), 873 (s), 851 (s), 845 (s), 824 (m), 764 (m), 712 (m), 685 (m), 641 (m), 591 (m), 579 (m), 556 (m), 534 (m), 510 (m), 482 (w), 443 (w), 415 (w). From DSC/TGA measurements, **5** is stable up to ∼250 °C.

$(H_2DABCO)_2[Mo_8O_{26}]\cdot 4H_2O$ (6). $(NH_4)_6[Mo_7O_{24}]\cdot 4H_2O$ (1.235 g, 1 mmol) was dissolved in 15 mL of water. After the addition of DABCO (0.196 g, 1.75 mmol), the pH was adjusted to 2 with 1 M HCl. The mixture was stirred at room temperature for 3 h and filtered to isolate a pale-yellow solid of **6**. The powder was washed with H_2O, EtOH, and Et_2O (yield: 85%). Anal. Calcd for $C_{12}H_{36}O_{30}N_4Mo_8$: C, 9.71; H, 2.44; N, 3.77; Mo, 51.72. Found: C, 9.90; H, 2.51; N, 3.75; Mo, 52.27. FT−IR (cm^{-1}): H_2O, 1630 (w), 1597 (w), H_2DABCO^{2+} cations, 1479 (m), 1461 (w), 1445 (w), 1391 (sh), 1366 (sh), 1327 (m), 1296 (w), 1261 (sh), 1112 (w), 1192 (sh), 1172 (sh), 1057 (m), 1034 (w), 1008 (w), 983 (w); ν(Mo═O, Mo−O−Mo) 955 (s), 940 (m), 927 (m), 903 (s), 869 (s), 850 (m), 804 (vs), 740 (m), 679 (vs), 639 (w), 583 (m), 552 (m), 523 (m), 482 (m), 442 (w), 427 (w), 407 (sh). From DSC/TGA measurements, **6** is stable up to ∼85 °C.

Table 1. Crystallographic Data for **1** and **2**

a. Physical, Crystallographic, and Analytical Data

	1	**2**
	$C_{18}H_{50}Mo_7N_6O_{28}$	$C_6H_{16}Mo_3N_2O_{11}$
crystal color	colorless	colorless
mol wt ($g\cdot mol^{-1}$)	1470.2	580
cryst syst	monoclinic	orthorhombic
space group	*Cc*	*Pnma*
T (K)	120	293
cell parameters		
a (Å)	17.064(4)	7.6028(5)
b (Å)	15.3018(3)	10.3658(9)
c (Å)	15.3674(4)	17.8759(12)
β (deg)	93.0850(11)	
V ($Å^3$)	4006.7(9)	1408.78(18)
Z	4	4
density (calcd, $g\cdot cm^{-3}$)	2.4364	2.7346
cryst description	block	lath
cryst size (mm^3)	∼0.32 × 0.26 × 0.18	∼0.6 × 0.016 × 0.0004

b. Data Collection

	1	**2**
monochromator	Bruker-Nonius Kappa CCD oriented graphite (002)	Bruker-Nonius Kappa CCD oriented graphite (002)
radiation	Mo $KL_{2,3}$ (λ = 0.71069 Å)	Mo $KL_{2,3}$ (λ = 0.71069 Å)
scan mode	φ and ω (1.7° per frame)	φ and ω (1.5° per frame)
hkl range	$-26 \le h \le 29$ $-21 \le k \le 25$ $-23 \le l \le 26$	$-12 \le h \le 11$ $-15 \le k \le 16$ $-28 \le l \le 27$
$\sin(\theta)/\lambda_{max}$ ($Å^{-1}$)	0.856	0.807
coverage (%) at θ_{max}	98	99

c. Data Reduction

	1	**2**
linear abs coeff (mm^{-1})	2.22	2.691
abs correction	analytical (Gaussian integration)	analytical (Gaussian integration)
T_{min}/T_{max}	0.653/0.825	0.671/0.999
no. of reflns	37496	25876
no. of indep reflns	18077	3215
criterions for obsd reflns	$I > 2\sigma(I)$	$I > 2\sigma(I)$
R_{int} (all)	0.0236	0.0899
average redundancy	2.1	3.6
no. of obsd reflns	33522	20272

d. Refinement

	1	**2**
refinement	F^2	F^2
F(000)	2840	1128
no. of reflns used in the refinement	18077	3215
no. of obsd reflns	15849	2717
no. of refined param	278	112
R^a(obsd)/R^a(all)	0.0471/0.0599	0.0439/0.0570
$R_w{}^a$(obsd)/$R_w{}^a$(all)	0.1444/0.1604	0.1244/0.1292
S(obsd)/*S*(all)	2.41/2.50	2.09/1.99
weighting scheme	$w = 1/(\sigma^2(\lvert F_o\rvert^2) + 0.0019\lvert F_o\rvert^2)$	$w = 1/(\sigma^2(\lvert F_o\rvert^2) + 0.0019\lvert F_o\rvert^2)$
secondary extinction coeff	none	none
difference Fourier residues ($e^-/Å^3$)	[−2.04, +3.17]	[−2.06, +2.39]

[a] $R = \sum||F_o| - |F_c||/\sum|F_o|$. $R_w = [\sum w(|F_o|^2 - |F_c|^2)^2/\sum w(|F_o|^4)]^{1/2}$.

(a) Synthesis of 6 from 1. 1 (736 mg, 0.5 mmol) was slurried in 15 mL of water, and the pH was adjusted to 2 with 1 M HCl. The mixture was stirred at room temperature for 3 h and filtered to isolate a pale-yellow solid of **6**. The powder was washed with H_2O, EtOH, and Et_2O (yield: 88%).

(b) Synthesis of 6 from 2. 2 (290 mg, 0.5 mmol) was slurried in 10 mL of water, and the pH was adjusted to 2 with 1 M HCl.

The mixture was stirred at room temperature for a few minutes and sealed in a 30-mL Teflon-lined autoclave (130 °C, 4 days, autogenous pressure). The resulting pale-yellow solid of **6** was isolated and washed with H_2O, EtOH, and Et_2O (yield: 95%).

(c) Synthesis of 6 from 3. **3** (768 mg, 0.5 mmol) was slurried in 15 mL of water, and the pH was adjusted to 2 with 1 M HCl. The mixture was stirred at room temperature for 3 h and filtered to isolate a pale-yellow solid of **6**. The powder was washed with H_2O, EtOH, and Et_2O (yield: 96%).

Structure Determination. Crystals of **1**, **2**, and **4** were glued at the tip of Lindemann capillaries by means of solvent-free glue. Diffraction intensities were collected at 120 K (**1**) and 293 K (**2** and **4**) on a Bruker-Nonius Kappa CCD diffractometer equipped with graphite-monochromated Mo $KL_{2,3}$ radiation (0.71073 Å), by using the φ- and ω-scan techniques and an Oxford cryostream cooler for the low-temperature achievement. The structures were initially solved by the Sir2004 direct methods,[15] completed and refined with the full-matrix least-squares technique using the Jana2000 program,[16] and drawn with the Diamond program.[17]

In the Mo-POM clusters, anisotropic atomic displacement parameters were only assigned to Mo atoms for **1** because of pseudosymmetry. Anisotropic atomic displacement parameters were assigned to all non-H atoms for **2**. A rigid-body description of the three H_2DABCO^{2+} entities was introduced for **1**. In addition, H atoms of H_2DABCO^{2+} were restrained in geometry, with riding atomic displacement parameters for **1** and **2**. H atoms of water molecules could not be introduced in the refinement. Crystallographic data and selected bond lengths for **1** and **2** are listed in Table 1. CCDC-625331 (**1**) and CCDC-625485 (**2**) contain the supplementary crystallographic data for this paper. These data can be obtained free of charge via the Internet at www.ccdc.cam.ac.uk/conts/retrieving.html (or from the Cambridge Crystallographic Data Centre, 12 Union Road, Cambridge CB21EZ, U.K.; fax (44) 1223-336-033; e-mail deposit@ccdc.cam.ac.uk). The structure of **4**, recently solved by Wang et al.,[18] was also reinvestigated, which led to slightly improved refinement parameters (see CCDC-625486 from the Cambridge Crystallographic Data Centre). Moreover, the purity of samples of **5** and **6** was checked by comparison of the experimental X-ray diffraction patterns with the simulated one issued from the single-crystal X-ray diffraction analysis of Harrison et al.[19] and Fang et al.[20−50]

Physical Measurements. Powder X-ray diffraction patterns were collected at room temperature on a Siemens D5000 diffractometer without a monochromator (Cu $KL_{3,2}$; $\lambda = 1.540598$ and 1.544390 Å; Bragg−Brentano geometry; linear detector; 2θ range = 8−60°). Elemental analyses of the solids were performed by the Service d'Analyze du CNRS, Vernaison, France. Fourier transform IR (FT−IR) spectra were recorded in the 4000−200 cm^{-1} range on a Bruker Vertex equipped with an attenuated total reflection device from Specac Eurolabo and computer control using the OPUS software. DSC/TGA analyses were measured by flowing dry argon with a heating and cooling rate of 5 °C·min^{-1} on a Setaram TG-DSC 111 between 20 and 800 °C. Room-temperature UV−vis diffuse-reflectance spectra were collected on a finely ground sample with a Cary 5G spectrometer (Varian). This instrument was equipped with a 60-mm-diameter integrating sphere and computer control using the "Scan" software. Diffuse reflectivity was then measured from 250 to 830 nm (5−1.5 eV) with a 2-nm step using Halon powder (from Varian) as the reference (100% reflectance). Before optical measurements, the sample powders were sifted at 50 μm to have quite a homogeneous distribution in the size of the particles and pressed in an adapted support to the integration sphere. The irradiation was realized outside the apparatus under a UV lamp [$\lambda_{exc} = 365$ nm (3.4 eV) or 254 nm (4.9 eV); $P = 12$ W, Fisher Bioblock labosi], at different durations, until no significant change in the reflectivity spectra was detected after an extra $^1/_2$ h of irradiation. The absorption (α/S) data were calculated from the reflectivity using the Kubelka−Munk function: $\alpha/S = (1 - R)^2/2R$, where R is the reflectivity at a given wavelength, α is the absorption coefficient, and S is the scattering coefficient. The latter was supposed to be particle size independent, as is expected for particles with diameter larger than a few micrometers. Practically, optical gaps are determined from a Kubelka−Munk transformed reflectivity spectrum as the intersection point between the energy axis and the line extrapolated from the linear portion of the absorption threshold.

Structure Description. (a) Single-Crystal X-ray Analyses of 1. The structure of **1** is composed of discrete $[Mo_7O_{24}]^{6-}$ clusters connected in a tridimensional array by H_2DABCO^{2+} cations and water molecules via hydrogen-bonding interactions. The well-known $[Mo_7O_{24}]^{6-}$ cluster consists of seven distorted edge-sharing $[MoO_6]$ octahedra, as shown in Figure 1a. The O sites fall broadly into four categories: terminal (O_t: O_7, O_8, O_{11}, O_{12}, O_{14}, O_{15}, O_{17}, O_{18}, O_{20}, O_{21}, O_{23}, O_{24}), twofold-coordinated (μ_2-O: O_1, O_5, O_9, O_{10},

(15) Burla, M. C.; Caliandro, R.; Camalli, M.; Carrozzini, B.; Cascarano, G. L.; De Caro, L.; Giacovazzo, C.; Polidori, G.; Spagna, R. SIR2004: an improved tool for crystal structure determination and refinement. *J. Appl. Crystallogr.* **2005**, *38*, 381−388.
(16) Petricek, V.; Dusek, M.; Palatinus, L. *JANA2000, the crystallographic computing system*; Institute of Physics, Academy of Sciences of the Czech Republic: Prague, Czech Republic, 2000.
(17) Brandenburg, K. *Diamond*, version 3; Crystal Impact GbR: Bonn, Germany, 2001.
(18) Wang, R.-Z.; Xiao, L.; Wang, Y.-Y.; Ma, C.-H.; Du, J.; Lin, X.; Liu, C.-L. *Solid State Sci.* **2006**, *8*, 77−81.
(19) Harrison, W. T. A.; Dussack, L. L.; Jacobson, A. J. *Acta Crystallogr.* **1996**, *C52*, 1075−1077.
(20) Fang, R.-Q.; Zhang, X.-M.; Wu, H.-S.; Ng, S. W. *Acta Crystallogr.* **2004**, *E60*, m359−m361.
(21) Lindqvist, I. *Acta Crystallogr.* **1950**, *3*, 159−160.
(22) Range, K.-J.; Fassler, A. *Acta Crystallogr.* **1990**, *C46*, 488−489.
(23) Don, A.; Weakley, T. J. R. *Acta Crystallogr.* **1981**, *B37*, 451−453.
(24) Xu, Y.; An, L.-H.; Koh, L.-L. *Chem. Mater.* **1996**, *8*, 814−818.
(25) Yamase, T. *J. Chem. Soc., Dalton Trans.* **1982**, 1987−1991.
(26) Lu, J.; Xu, Y. *Chem. Mater.* **1998**, *10*, 4141−4147.
(27) Ohashi, Y.; Yanagi, K.; Sasada, Y.; Yamase, T. *Bull. Chem. Soc. Jpn.* **1982**, *55*, 1254−1260.
(28) Toraya, H.; Marumo, F.; Yamase, T. *Acta Crystallogr.* **1984**, *B40*, 145−150.
(29) Roman, P.; José, A. S.; Luque, A.; Guitierrez-Zorilla, J. M. *Acta Crystallogr.* **1994**, *C50*, 1031−1034.
(30) Khan, I.; Chen, Q.; Zubieta, J. *Inorg. Chim. Acta* **1993**, *213*, 325−327.
(31) Roman, P.; Luque, A.; Aranzabe, A.; Guttierrez-Zorrilla, J. M. *Polyhedron* **1992**, *11*, 2027−2038.
(32) Nelson, J. R.; Narducci, Sarjeant, A.; Norquist, J. *Acta Crystallogr.* **2006**, *E62*, m1448−m1450.
(33) Roman, P.; Guitierrez-Zorilla, J. M.; Martinez-Ripoll, M.; Garcia-Blanco, S. *Transition Met. Chem.* **1986**, *11*, 143−150.
(34) Lasocha, W.; Jansen, J.; Schenk, H. *J. Solid State Chem.* **1995**, *117*, 103−107.
(35) Roman, P.; Guitierrez-Zorilla, J. M.; Luque, A.; Martinez-Ripoll, M. *Z. Kristallogr.* **1985**, *173*, 283−292.
(36) Sun, D.; Zhang, H.; Zhang, J.; Zheng, G.; Yu, J.; Gao, S. *J. Solid State Chem.* **2007**, *180*, 276−282.
(37) Niu, J.-Y.; You, X.-Z.; Fun, H.-K.; Zhou, Z.-Y.; Yip, B.-C. *Polyhedron* **1996**, *15*, 1003−1008.
(38) Veltman, T. R.; Stover, A. K.; Narducci Sarjeant, A.; Min Ok, K.; Shiv Halasyamani, P.; Norquist, A. J. *Inorg. Chem.* **2006**, *45*, 5529−5537.
(39) Kong, Z.; Weng, L.; Tan, D.; He, H.; Zhang, B.; Kong, J.; Yue, B. *Inorg. Chem.* **2004**, *43*, 5676−5680.
(40) Hagrman, D.; Warren, C. J.; Haushalter, R. C.; Seip, C.; O'Connor, C. J.; Rarig, R. S., Jr.; Johnson, K. M., III; LaDuca, R. L., Jr.; Zubieta, J. *Chem. Mater* **1998**, *10*, 3294−3297.
(41) Benchrifa, R.; Leblanc, M.; de Pape, R. *Eur. J. Solid State Inorg. Chem.* **1989**, *26*, 593.

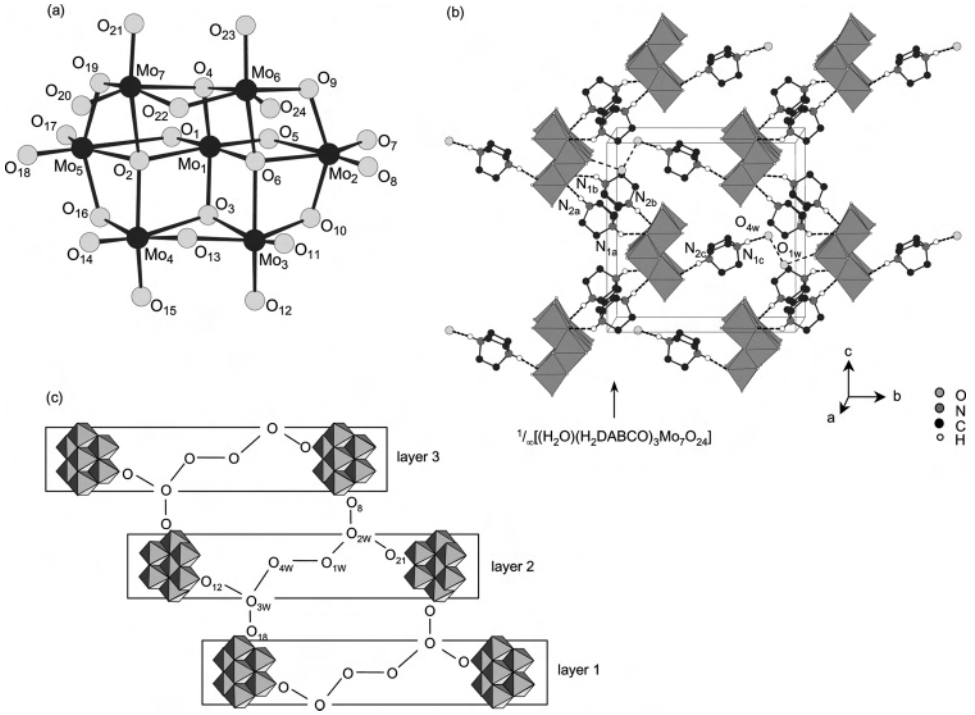

Figure 1. (a) Ball-and-stick representation of the $[Mo_7O_{24}]^{6-}$ anion in **1** showing the labeling scheme. (b) Representation of the $^1/_\infty[(H_2O)(H_2DABCO)_3Mo_7O_{24}]$ chains oriented along the *c* axis and connected to each other via an $O_{4w}\cdots O_{1w}$ bridge to form $^2/_\infty[(H_2O)_2(H_2DABCO)_3Mo_7O_{24}]$ layers. (c) Schematic representation of the interconnection of the $^2/_\infty[(H_2O)_2(H_2DABCO)_3Mo_7O_{24}]$ layers via both water molecules O_{2w} and O_{3w}. The four water molecules O_{iw} are hydrogen-bonded through an $O_{3w}\cdots O_{4w}\cdots O_{1w}\cdots O_{2w}$ bridge in one layer. The H_2DABCO^{2+} fragments that link the $[Mo_7O_{24}]^{6-}$ clusters in the $^2/_\infty[(H_2O)_2(H_2DABCO)_3Mo_7O_{24}]$ layers are not represented for clarity.

Table 2. Hydrogen-Bonding Geometry (Å, deg) in **1**, **2**, and **4**

N−H···O	N−H	H···O	N···O	N−H···O
		Compound **1**		
$N_{1a}-H_{1a}\cdots O_{19}$	0.93	2.09	2.841(6)	135.82
$N_{2a}-H_{2a}\cdots O_{16}$	0.93	1.63	2.561(9)	172.03
$N_{1b}-H_{2b}\cdots O_{10}$	0.93	1.97	2.783(6)	144.82
$N_{2b}-H_{2b}\cdots O_9$	0.93	1.61	2.543(9)	172.02
$N_{1c}-H_{2c}\cdots O_{4w}$	0.93	1.76	2.687(5)	169.12
$N_{2c}-H_{2c}\cdots O_{13}$	0.93	1.80	2.727(8)	170.84
		Compound **2**		
$N_1-H_1\cdots O_5$	0.92	1.78	2.674(6)	161.44
$N_2-H_2\cdots O_{\_w}$	0.92	2.00	2.744	136.55
		Compound **4**		
$N_1-H_1\cdots O_{12}$	0.92	1.74	2.644(3)	164.14
$N_2-H_2\cdots O_7$	0.92	1.86	2.676(3)	145.42
$N_3-H_{20}\cdots O_9$	0.92	1.91	2.764(3)	153.67
$N_3-H_{19}\cdots O_{14}$	0.92	2.00	2.898(3)	164.71

O_{13}, O_{16}, O_{19}, O_{22}), threefold-coordinated (μ_3-O: O_3, O_4), and fourfold-coordinated (μ_4-O: O_2, O_6). Each $[MoO_6]$ polyhedron has three kinds of Mo−O bonds: two short [1.675(5)−1.766(5) Å], two medium [1.877(5)−1.991(3) Å], and two long [2.112(6)−2.689(6) Å]. All Mo centers have two O_t atoms with a *cis*-dioxo conformation, except Mo_1, which sets at the central position in the cluster. Nevertheless, the Mo_1-O_1 and Mo_1-O_5 distances are more typical of O_t bond lengths [1.749(6) and 1.763(5) Å, respectively] than μ_2-O. Subjectively, the structure of **1** may be described as follows: as shown in Figure 1b, $[Mo_7O_{24}]^{6-}$ anions are connected to each other by two H_2DABCO^{2+} cations, with N−O distances ranging from 2.543(9) to 2.841(6) Å (see Table 2), to form $^1/_\infty[(H_2DABCO)_2Mo_7O_{24}]^{2-}$ zigzag chains along the *c* axis. The third H_2DABCO^{2+} cation is hooked up to the aforementioned chain via a $N_{2c}\cdots H_{2c}\cdots\mu^2$-$O_{13}$ interaction with a $N_{2c}-O_{13}$ distance of 2.727(8) Å, while the second nitrogen atom N_{1c} is bonded to a water molecule O_{4w}. The as-defined $^1/_\infty[(H_2O)(H_2DABCO)_3Mo_7O_{24}]$ chains are connected to each other via a $O_{4w}\cdots O_{1w}$ hydrogen bridge to form $^2/_\infty[(H_2O)_2(H_2DABCO)_3Mo_7O_{24}]$ layers running in the *bc* plane. The connection between the layers is ensured via the two other water molecules O_{3w} and O_{2w}, as shown in Figure 1c. In one slab, the four water molecules O_{iw} are hydrogen-bonded through a $O_{3w}\cdots O_{4w}\cdots O_{1w}\cdots O_{2w}$ bridge. At the same time, O_{3w} and O_{2w} link two $[Mo_7O_{24}]^{6-}$ clusters of two adjacent layers via O_t atoms O_{12}, O_{18} and O_8, O_{21}, respectively, with O_{iW}-O distances ranging from 2.784(7) to 2.844(9) Å.

(b) Single-Crystal X-ray Analyses of 2. Compound **2** consists of polymeric $^1/_\infty[Mo_3O_{10}]^{2-}$ chains assembled by H_2DABCO^{2+} cations and water molecules via hydrogen-bonding interactions. The inorganic part is built from $[Mo_6O_{20}]$ blocks displayed in Figure 2a. It is composed of six edge-shared distorted MoO_6 octahedra within the two crystallographically independent Mo_1 and Mo_2 atoms having three kinds of Mo−O bonds: two short [1.693(3)−1.711(3) Å] in the cis position typical of $Mo-O_t$ bonds, two medium [1.916(4)−1.969(3) Å], and two long [2.231(2)−2.269(2) Å]. $[Mo_6O_{20}]$ blocks condense to give rise to infinite zigzag $^1/_\infty[Mo_3O_{10}]^{2-}$ chains oriented along the *a* axis, as shown in Figure 2b. H_2DABCO^{2+} cations are connected to the μ^3-O atom (O_5) of the $^1/_\infty[Mo_3O_{10}]^{2-}$ chains via a short hydrogen bond with a N_1-O_5 distance of 2.674(6) Å, while its second protonated nitrogen atom N_2 is linked to the oxygen atom O_W of the water molecule with a distance of 2.741(7) Å. These as-defined, infinite $^1/_\infty[(H_2O)(H_2DABCO)Mo_3O_{10}]$ chains are associated all together to form a three-dimensional edifice thanks to interaction of each water molecule with two extra $^1/_\infty[(H_2O)(H_2DABCO)Mo_3O_{10}]$ chains via hydrogen-bonding interactions with a $O_W\cdots O_3$ distance of 2.882(4) Å, as displayed in Figure 2c. Consequently, to some extent, the structure of **2** can also be viewed as the regular stacking of inorganic $^2/_\infty[(H_2O)Mo_3O_{10}]^{2-}$ layers along the *c* axis interspaced by H_2DABCO^{2+} cations.

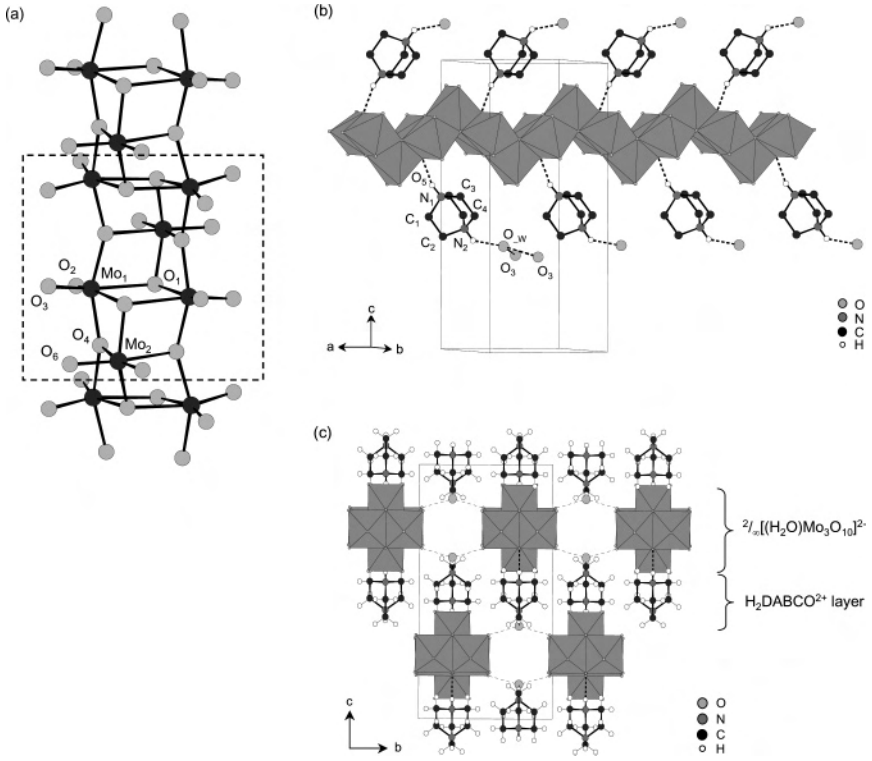

Figure 2. (a) Ball-and-stick representation of the $[Mo_6O_{20}]$ block in the $^1/_\infty[Mo_3O_{10}]^{2-}$ chain of **2** showing the labeling scheme. (b) Representation of the assembly of H_2DABCO^{2+} cations connected to the infinite $^1/_\infty[Mo_3O_{10}]^{2-}$ chain and water molecule via hydrogen-bonding interactions (dotted lines). For better clarity, all H atoms except those connected to N atoms of the H_2DABCO^{2+} cations are not shown. (c) Representation of the stacking of both inorganic $^2/_\infty[(H_2O)Mo_3O_{10}]^{2-}$ and organic H_2DABCO^{2+} layers. Dotted lines represent the hydrogen-bonding interactions between O_w of the water molecule and the O_3 atom of $^1/_\infty[Mo_3O_{10}]^{2-}$ clusters.

(c) Structural Description of 4 and 5. Both crystal structures of **4** and **5** present pronounced similarities. That of **4** consists of $[Mo_8O_{27}]^{6-}$ anions connected in network by H_2DABCO^{2+} and H_2pipz^{2+} cations via hydrogen-bonding interactions. The anions are built from $[Mo_8O_{28}]$ subunits, composed of eight edge-shared distorted $[MoO_6]$ octahedra, as shown in Figure 3a. The $[Mo_8O_{28}]$ blocks condense via the sharing of one common vertex (O_{11}) to form infinite $^1/_\infty[Mo_8O_{27}]^{6-}$ chains running along the *a* axis, as displayed in Figure 3b. These chains are connected by H_2pipz^{2+} cations to form $^2/_\infty[(H_2pipz)Mo_8O_{27}]^{4-}$ layers parallel to the *ac* plane, via hydrogen-bonding interactions with the O_t atoms O_9 and O_{14} of four $[Mo_8O_{28}]$ subunits (O_9-H_{20} and $O_{14}-H_{19}$ bond lengths are 1.9089(18) and 2.0003(18) Å, respectively). An identical arrangement is observed in **5**[19] with slightly shorter interatomic O−H distances [1.8403(10) and 1.8535(9) Å]. As displayed schematically in Figure 3c, these layers are interspaced by H_2DABCO^{2+} and H_2pipz^{2+} cations in **4** and **5**, respectively, with the occurrence of hydrogen bonding. Alternatively, the structures of **4** and **5** can be regarded as the assembly of infinite $^1/_\infty[Mo_8O_{27}]^{6-}$ chains connected by cations belonging to two distinguishable cationic subnetworks, hereafter labeled lattice 1 and lattice 2 containing H_2DABCO^{2+} and H_2pipz^{2+} and containing H_2pipz^{2+} only in **4** and **5**, respectively (Figure 4). This description will be favored in the interpretation task of the optical properties of the materials (vide infra). Let us mention that no crystal suitable for X-ray determination has been prepared for **3** until now. Nevertheless, on the basis of IR spectroscopy (vide infra), **3** may be viewed as deriving from **4** and **5** with H_2DABCO^{2+} and NH_4^+ species housed in lattice 1 and lattice 2, respectively.

Factors Governing the Stabilization of $[Mo_7O_{24}]^{6-}$ Clusters and Infinite $^1/_\infty[Mo_8O_{26}]^{4-}$, $^1/_\infty[Mo_8O_{27}]^{6-}$, and $^1/_\infty[Mo_3O_{10}]^{2-}$ Chains in the Solid State. The reactivity of the heptamolybdate toward DABCO and pipz led to the synthesis of six organic−inorganic hybrid materials with four different Mo-POM blocks (i.e., one discrete $[Mo_7O_{24}]^{6-}$ anion in **1** and three infinite chains, namely, $^1/_\infty[Mo_3O_{10}]^{2-}$ in **2**, $^1/_\infty[Mo_8O_{27}]^{6-}$ in **3**−**5**, and $^1/_\infty[Mo_8O_{26}]^{4-}$ in **6**). All of them can be obtained in ambient conditions, except **2**, which requests strictly hydrothermal conditions. These aforementioned mineral fragments have already been observed in several solid materials when associated with a large variety of organic countercations (see Table 3). However, so far, their rational design, like a lot of material containing a specific Mo-POM block, still remains an unresolved problem to address. Commonly, the stabilization of a specific isopolyoxomolybdate is correlated to the nature of the organic cation deemed to play the role of a structure-directing reagent. Of course, the factors influencing the stabilization of a new mineral edifice cannot be limited to the only role of the template, and parameters such as the pH, Mo concentration, amine/Mo ratio, ionic strength, and temperature have to be taken into account. Nowadays, most reported compounds have been isolated for only discrete values of these parameters without a discussion of their interdependence. For this purpose, the large structural variety observed in the DABCO/$[Mo_7O_{24}]^{6-}$ system may serve as an attempt to clearly dissociate the role of the organic countercation, pH, DABCO/$[Mo_7O_{24}]^{6-}$ ratio, and temperature on the stabilization of the mineral species.

The synthesis conditions of compounds **1**−**6** from $[Mo_7O_{24}]^{6-}$, DABCO, and pipz are illustrated in Scheme 1. The stabilization of the different Mo-POM blocks, which results from a competition between dissolution/precipitation and oxolation/condensation mechanisms, is discussed in terms of the pH, DABCO/$[Mo_7O_{24}]^{6-}$ molecular ratio (hereafter labeled N), and temperature. For brevity, a couple of parameters (*N*,pH) are systematically associated with each compound.

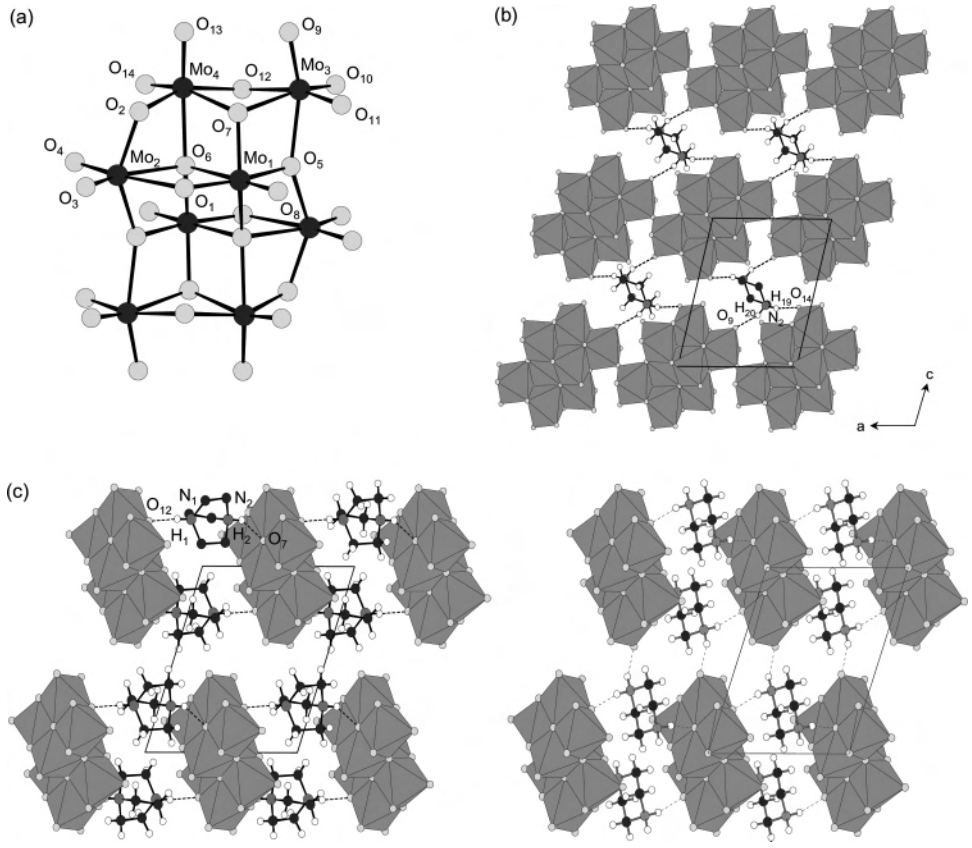

Figure 3. (a) Ball-and-stick representation of the $[Mo_8O_{28}]$ block in the $^1/_\infty[Mo_8O_{27}]^{6-}$ chain of **4** showing the labeling scheme. (b) Representation of the $^1/_\infty[Mo_8O_{27}]^{6-}$ chains connected by H_2pipz^{2+} cations to form $^2/_\infty[(H_2pipz)Mo_8O_{27}]^{4-}$ layers. (c) Representation of the $^1/_\infty[Mo_8O_{27}]^{6-}$ chains parallel to the propagation axis and connected by the H_2DABCO^{2+} cations in **4** (left) and by the H_2pipz^{2+} cations in **5** (right).

(a) $[Mo_7O_{24}]^{6-}$ Block. Compound **1** (3,4.5) is obtained quantitatively from an ammonium heptamolybdate solution ([Mo] = 0.47 M) as in eq 1 via acidification of the mother solution while maintaining the integrity of the $[Mo_7O_{24}]^{6-}$ blocks. Its formation results from the instantaneous metathesis of NH_4^+ cations by diprotonated DABCO with precipitation due to a change in the solubility product. At room temperature, this reaction is achieved for pH 4.5 and $N \geq 3$, with $N = 3$ being the smaller ratio requested to ensure a complete substitution with respect of the charge balance. For pH $\geq$4.5, partial substitution with stabilization of $(NH_4)_{6-2x}(H_2DABCO)_x[Mo_7O_{24}]\cdot 4H_2O$ series members ($0 < x < 3$) has never been accomplished, probably because of the too fast precipitation reaction of **1**.

$$(NH_4)_6[Mo_7O_{24}]\cdot 4H_2O + 3DABCO + 6H^+ \rightarrow \mathbf{1} + 6NH_4^+ \quad (1)$$

(b) $^1/_\infty[Mo_8O_{27}]^{6-}$ Block. For $N = 1.75$, the conversion from the heptamolybdate anion to the $[Mo_8O_{27}]^{6-}$ cluster occurs by decreasing the pH to 4, and **3** (1.75,4) is precipitated quantitatively according to eq 2. In this case, the use of $(NH_4)_6[Mo_7O_{24}]\cdot 4H_2O$ as the starting material induces the presence of NH_4^+ cations in the solution, which can act as a charge-compensating reagent in the case of a default of DABCO. For N values ranging from 1.75 to 3, a mixture of **1** and **3** has been systematically obtained and characterized by powder X-ray diffraction analyses.

$$8[Mo_7O_{24}]^{6-} + 14DABCO + 34H^+ + 14NH_4^+ + 25H_2O \rightarrow 7(\mathbf{3}) \quad (2)$$

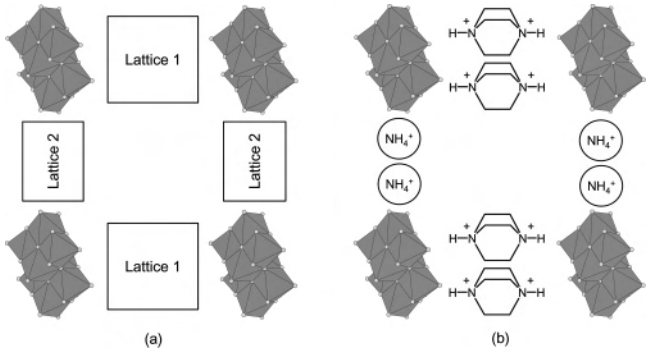

Figure 4. (a) Schematic representation of the arrangement of the mineral and organic components in **4** and **5**, which evidences the occurrence of two types of organic lattices. (b) Suspected structural arrangement in **3**. For simplicity, water molecules are not displayed.

The stability of Mo-POMs in an aqueous solution is strongly pH-dependent. Several theoretical models have been proposed to account for the protonation and condensation reactions in the mother liquor that may occur upon acidification of the molybdate solution.[51−54] Nevertheless, the observation of some Mo-POMs in the solid state contradicts these models, probably because their existence in solution remains questionable and their stabilization in the solid state implies unidentified steps. This is particularly the case for the $^1/_\infty[Mo_8O_{26}]^{4-}$, $^1/_\infty[Mo_3O_{10}]^{2-}$, and $^1/_\infty[Mo_8O_{27}]^{6-}$ polymers. However, the occurrence of these $Mo_xO_y^{n-}$ anions may be approached via formal acid−base equilibria (eqs 3−5), which allow one to follow their prospective formation

Table 3. List of Compounds Containing $[Mo_7O_{24}]^{6-}$ Discrete Entities, $^1/_\infty[Mo_3O_{10}]^{2-}$, $^1/_\infty[Mo_8O_{26}]^{4-}$, and $^1/_\infty[Mo_8O_{27}]^{6-}$ Chains

$[Mo_7O_{24}]^{6-}$	ref	$^1/_\infty[Mo_3O_{10}]^{2-}$	ref
$(NH_4)_6[Mo_7O_{24}]\cdot 4H_2O$	21	$(NH_4)_2[Mo_3O_{10}]$	22
$(CH_6N_3)_6[Mo_7O_{24}]\cdot H_2O$	23	$Na(NH_4)[Mo_3O_{10}]$	24
$(n-C_3H_{10}N)_6[Mo_7O_{24}]\cdot 3H_2O$	25	$(CH_6N_3)(NH_4)[Mo_3O_{10}]$	26
$(i-C_3H_{10}N)_6[Mo_7O_{24}]\cdot 3H_2O$	27	$(C_2H_8N)_2[Mo_3O_{10}]\cdot H_2O$	28
$(C_4H_{12}N)_6[Mo_7O_{24}]\cdot 7H_2O$	29	$(C_2H_{10}N_2)[Mo_3O_{10}]$	30
$(C_4H_{16}N_3)_2[Mo_7O_{24}]\cdot 4H_2O$	31	$(C_5H_7N_2)_2[Mo_3O_{10}]$	32
$(C_5H_7N_2)_6[Mo_7O_{24}]\cdot 3H_2O$	33	$(C_6H_5NH_3)_2[Mo_3O_{10}].4H_2O$	34
$(C_5H_7N_2)_6[Mo_7O_{24}]\cdot 6H_2O$	35	$(C_6H_{18}N_2)_2[Mo_3O_{10}]$	36
$(C_6H_{18}N_2)_3[Mo_7O_{24}]\cdot 4H_2O$	37	$(C_7H_{16}N_2)[Mo_3O_{10}]\cdot H_2O$	38
		$[Cu(4,4'\text{-bipy})(H_2O)Mo_3O_{10}]\cdot H_2O$	39
		$[Cu_2(pyrd)Mo_3O_{10}]$	40

$^1/_\infty[Mo_8O_{26}]^{4-}$	ref	$^1/_\infty[Mo_8O_{27}]^{6-}$	ref
$(NH_4)_4[Mo_8O_{26}]$	41	$(NH_4)_6[Mo_8O_{27}]\cdot 4H_2O$	42
$(C_3H_{12}N_2)_2[Mo_8O_{26}]\cdot H_2O$	43	$(C_4H_{12}N_2)_3[Mo_8O_{27}]$	19
$(C_3H_{12}N_2)_2[Mo_8O_{26}]\cdot 2H_2O$	44	$(C_6H_{14}N_2)_2(C_4H_{12}N_2)[Mo_8O_{27}]$	18
$(C_4H_{14}N_2)_2[Mo_8O_{26}]\cdot 2H_2O$	45	$Sm_2(H_2O)_{12}[Mo_8O_{27}]\cdot 6H_2O$	46
$(C_5H_7N_2)_2[Mo_8O_{26}]$	47	$Eu_2(H_2O)_{12}[Mo_8O_{27}]\cdot 6H_2O$	48
$(C_6H_8N)_4[Mo_8O_{26}]$	49	$Cu_2(C_6H_{13}N_2)_2[H_2Mo_8O_{27}]\cdot 4H_2O$	50
$(C_6H_{14}N_2)_2[Mo_8O_{26}]\cdot 4H_2O$	14, 20		
$(C_6H_{14}N_2)_2[Mo_8O_{26}]\cdot 4.66H_2O$	14		
$(C_6H_{18}N_2)_2[Mo_8O_{26}]$	24		

from an acidified heptamolybdate aqueous solution in a specific pH range.

$$8[Mo_7O_{24}]^{6-} + 6H^+ \leftrightarrows 7[Mo_8O_{27}]^{6-} + 3H_2O \quad (3)$$

$$3[Mo_8O_{27}]^{6-} + 2H^+ \leftrightarrows 8[Mo_3O_{10}]^{2-} + H_2O \quad (4)$$

$$8[Mo_3O_{10}]^{2-} + 4H^+ \leftrightarrows 3[Mo_8O_{26}]^{4-} + 2H_2O \quad (5)$$

Namely, the conversion pathway of the $[Mo_7O_{24}]^{6-}$ cluster into the $[Mo_8O_{27}]^{6-}$ cluster may be envisioned as follows: if the discrete $[Mo_7O_{24}]^{6-}$ anion is reported to be the predominant solute species in an aqueous solution for Mo concentrations up to 10^{-3} mol·L^{-1} and at a pH ranging from 7 to 4.5, around pH 4 this entity is in thermodynamical equilibrium with two octamolybdate species, namely, γ-$[Mo_8O_{25}(OH)_3]^{5-}$ and β-$[Mo_8O_{26}]^{4-}$, as in eqs 6 and 7, respectively.[53]

$$8[Mo_7O_{24}]^{6-} + 13H^+ + 4H_2O \leftrightarrows 7\gamma\text{-}[Mo_8O_{25}(OH)_3]^{5-} \quad (6)$$

$$8[Mo_7O_{24}]^{6-} + 20H^+ \leftrightarrows 7\beta\text{-}[Mo_8O_{26}]^{4-} + 10H_2O \quad (7)$$

The structure of the γ-$[Mo_8O_{25}(OH)_3]^{5-}$ anion is unknown, but it is assumed to be isostructural with the one of the γ-$[Mo_8O_{26}(OH)_2]^{6-}$ clusters,[55] which was crystallized from an aqueous solution with isopropylammonium countercations.[56] The conformation of the eight MoO_6 octahedra in these anions turns out to be very similar to the one observed in the γ-$[Mo_8O_{28}]$ building block of the $^1/_\infty[Mo_8O_{27}]^{6-}$ chain. So, the formation of the γ-$[Mo_8O_{26}(OH)_2]^{6-}$ block as an intermediary species between 0D $[Mo_7O_{24}]^{6-}$ and 1D $[Mo_8O_{27}]^{6-}$ entities may be reasonably suspected during the formation of **3**. The self-condensation of the γ-$[Mo_8O_{26}(OH)_2]^{6-}$ entities may lead to the infinite $^1/_\infty[Mo_8O_{27}]^{6-}$ chains as in eq 8.

$$n[Mo_8O_{26}(OH)_2]^{6-} \rightarrow [Mo_8O_{27}]_n^{6n-} + nH_2O \quad (8)$$

Because of the lack of a monocrystal suitable for X-ray diffraction study, the structure of **3** remains unknown. However, the presence of the infinite $^1/_\infty[Mo_8O_{27}]^{6-}$ chains has been unambiguously characterized by IR spectroscopy. The spectrum of **3** shows the absorption bands of H_2DABCO^{2+} cations located between 1500 and 1000 cm^{-1} in the same range as those observed in compounds **1**, **2**, **4**, and **6**. In addition, a strong absorption band at 1402 cm^{-1} is attributed to the N−H stretching vibration mode of NH_4^+ cations present in the framework. The polymeric $^1/_\infty[Mo_8O_{27}]^{6-}$ cluster in **3** has been characterized by the absorption bands related to ν(Mo=O$_t$) and ν(Mo−O−M*o*) vibrations below 1000 cm^{-1}. As shown in Table 4, these frequencies are similar to those observed for **4** and **5**. Notice that the IR spectrum of **3** is totally different from that of $(^i PrNH_3)_6[Mo_8O_{26}(OH)_2]\cdot 2H_2O$,[56] which rules out definitively the possible stabilization of isolated $[Mo_8O_{28}]$ entities.

Another piece of information about the structure of **3** can be deduced from structural analyses of **4**, **5**, and $(NH_4)_6[Mo_8O_{27}]\cdot 4H_2O$.[42] Both structures of **4** and **5** can be described as summed up in Figure 4. The infinite $^1/_\infty[Mo_8O_{27}]^{6-}$ chains displayed in a view parallel to the propagation axis are spaced out by two types of cationic lattices. Lattice 1 is occupied by H_2DABCO^{2+} or H_2pipz^{2+} cations in **4** and **5**, while lattice 2 is strictly occupied by H_2pipz^{2+}. A similar arrangement of the N atoms in lattice 2 is observed in the structure of $(NH_4)_6[Mo_8O_{27}]\cdot 4H_2O$ within two NH_4^+ cations replacing the diprotonated pipz. In all of these structures, each N atom present in lattice 2 connects two successive $[Mo_8O_{28}]$ blocks of the chain with at least two hydrogen bonds acting like a pincer to rigidify the $^1/_\infty[Mo_8O_{27}]^{6-}$ polymers (Figure 5). Although their structures present more differences from those of **4**, **5**, and $(NH_4)_6[Mo_8O_{27}]\cdot 4H_2O$, a similar effect is observed for the metallic and lanthanide cations in $Cu_2(HDABCO)_2[H_2Mo_8O_{27}]\cdot 4H_2O$[50] and $(Ln(H_2O)_6)_2[Mo_8O_{27}]\cdot 6H_2O$ (Ln = Eu,[48] Sm[46]), respectively. With regard to these observations, we may propose a localization of the countercations in **3** similar to those of **4** and **5**; i.e., the two H_2DABCO^{2+} cations and the two NH_4^+ cations may occupy lattice 1 and lattice 2, respectively. Because of the tertiary character of the N atoms in the H_2DABCO^{2+} cation, it cannot play the role of pincer as in lattice 2, which goes along with the stabilization of $[Mo_7O_{24}]^{6-}$, $^1/_\infty[Mo_8O_{26}]^{4-}$, and $^1/_\infty[Mo_3O_{10}]^{2-}$ arrangements in the solid state only with H_2DABCO^{2+} as countercations, while attempts to isolate hypothetical $(H_2DABCO)_3[Mo_8O_{27}]\cdot xH_2O$ were always unsuccessful.

The stoichiometric addition of both DABCO and pipz in an ammonium heptamolybdate solution with *N* and pH values similar to those of compound **3** leads to the quantitative formation of **4** (1.75,4) as in eq 9. Compound **5** is obtained similarly from the addition of a stoichiometric amount of pipz to an ammonium heptamolybdate solution at pH 4 according to eq 10. Both compounds **4** and **5** were obtained hydrothermally with average yields from the addition of DABCO and/or pipz to an aqueous mixture of MoO_3 at 170 and 180 °C, respectively. The synthesis

(42) Böschen, V. I.; Buss, B.; Krebs, B. *Acta Crystallogr.* **1974**, *B30*, 48−56.
(43) Chakrabarti, S.; Natarajan, S. *Cryst. Growth Des.* **2002**, *2*, 333−335.
(44) Xiao, D.; An, H.; Wang, E.; Xu, L. *J. Mol. Struct.* **2005**, *738*, 217−225.
(45) Thorn, K. J.; Narducci Sarjeant, A.; Norquist, A. J. *Acta Crystallogr.* **2005**, *E61*, m1665−m1667.
(46) Yamase, T.; Ozeki, T.; Kawashima, I. *Acta Crystallogr.* **1995**, *C51*, 545−547.
(47) Nelson, J. R.; Narducci Sarjeant, A.; Norquist, A. J. *Acta Crystallogr.* **2006**, *E62*, m1731−m1733.
(48) Yamase, T.; Naruke, H. *J. Chem. Soc., Dalton Trans.* **1991**, *2*, 285−292.
(49) Modec, B.; Brencic, J. V.; Zubieta, J. *Inorg. Chem. Commun.* **2003**, *6*, 506−512.
(50) Fang, R.-Q.; Zhao, Y.-F.; Zhang, X.-M. *Inorg. Chim. Acta* **2006**, *359*, 2023−2028.
(51) Tytko, K. H.; Baethe, G.; Hirschfeld, E. R.; Mehmke, K.; Stellhorn, D. *Z. Anorg. Allg. Chem.* **1983**, *503*, 43−66.
(52) Tytko, K. H.; Baethe, G.; Cruywagen, J. J. *Inorg. Chem.* **1985**, *24*, 3132−3136.

Scheme 1

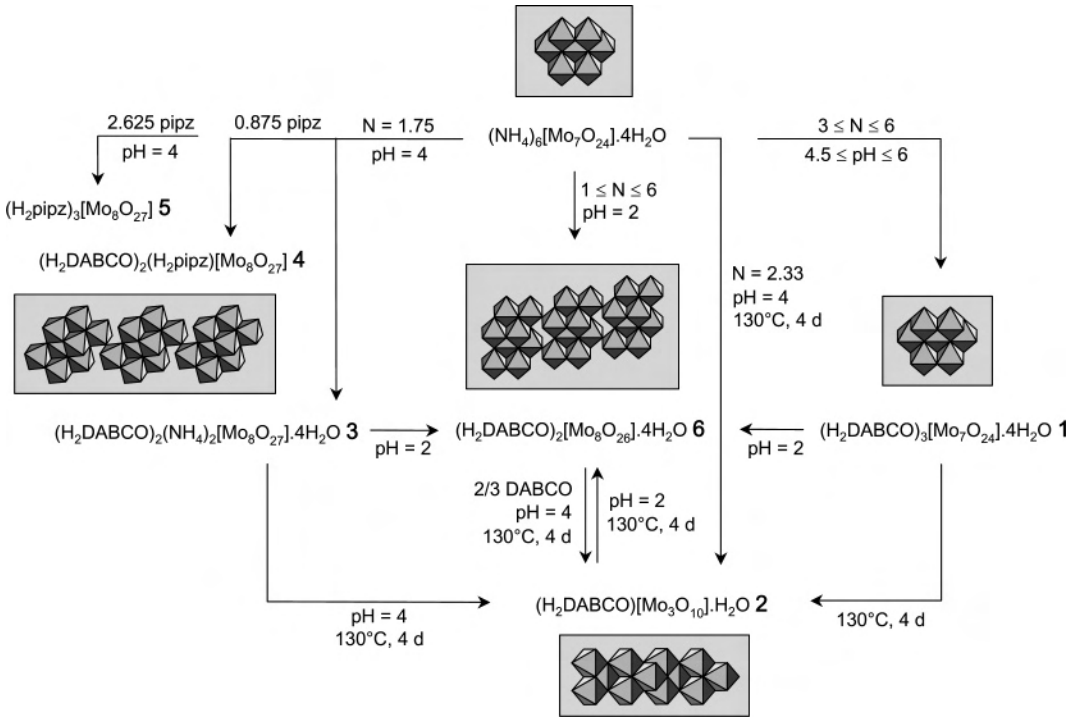

Table 4. Selected Absorption Frequencies (cm^{-1}) Related to the $^1/_\infty[Mo_8O_{27}]^{6-}$ Cluster in **3**−**5**

3	4	5
941, 926, 909	932	933, 900
869	875−865	873−852
837	839	840
769	774	763
693	701	712, 685
645	648	641
580, 533, 500	577, 553, 536, 507	579, 560, 534, 511
474	474	483
441	438	444

of **4** and **5** described in the present paper shows unambiguously that hydrothermal conditions are not necessary.

$$8[Mo_7O_{24}]^{6-} + 14\text{DABCO} + 7\text{pipz} + 48H^+ \rightarrow 7(\mathbf{4}) + 3H_2O \quad (9)$$

$$8[Mo_7O_{24}]^{6-} + 21\text{pipz} + 48H^+ \rightarrow 7(\mathbf{5}) + 3H_2O \quad (10)$$

(c) $^1/_\infty[Mo_8O_{26}]^{4-}$ Block. Compound **6** (1.75,2) has been obtained with a high yield as in eq 11. Its structure is similar to that reported in the literature (see Table 3) and contains polymeric $^1/_\infty[Mo_8O_{26}]^{4-}$ clusters built from the γ-$[Mo_8O_{28}]$ subunits described above, connected by the sharing of two common vertices, as shown in Figure 5. This compound was first obtained hydrothermally by Fang et al.[20] in moderate yield from the addition of DABCO to an aqueous slurry of MoO_3 at 180 °C. Recently, we reported the synthesis and X-ray characterization of one other commensurate $(H_2DABCO)_2[Mo_8O_{26}]\cdot 4H_2O$ phase, which drifts mainly from the structure of **6** by different orientations of H_2DABCO^{2+} cations toward the inorganic fragment and one incommensurat e $(H_2DABCO)_2[Mo_8O_{26}]\cdot 4H_2O$ compound.[14] As is the case for compounds **4** and **5**, the present study shows that **6** can be obtained quantitatively without the need for hydrothermal conditions.

Similarly to the $^1/_\infty[Mo_8O_{27}]^{6-}$ chains, the presence of the γ-$[Mo_8O_{26}(OH)_2]^{6-}$ anion as an intermediary species between 0D $[Mo_7O_{24}]^{6-}$ and 1D $[Mo_8O_{26}]^{4-}$ entities may be suspected during the formation of **6**, but its condensation by the sharing of two common vertices requests more severe acidic conditions as in eq 12.

$$8[Mo_7O_{24}]^{6-} + 14\text{DABCO} + 48H^+ + 18H_2O \rightarrow 7(\mathbf{6}) \quad (11)$$

$$n[Mo_8O_{26}(OH)_2]^{6-} + 2nH^+ \rightarrow [Mo_8O_{26}]_n^{4n-} + 2nH_2O \quad (12)$$

Compound **6** has been systematically isolated from an ammonium heptamolybdate solution at pH 2 for *N* values ranging from 1 to 6, in ambient conditions or by hydrothermal conditions, showing that stabilization of the $^1/_\infty[Mo_8O_{26}]^{4-}$ chains needs systematically strong acidification conditions, which agrees with eqs 3−5. In the same way, the conversion of **1** (eq 13), **2** (eq 14), and **3** (eq 15) to **6** has been highlighted by acidifying to pH 2 slurries of each compound in an aqueous solution. Because of its very low solubility in water, the conversion of **2** from **6** is limited in ambient conditions but occurs quantitatively using hydrothermal conditions at 130 °C.

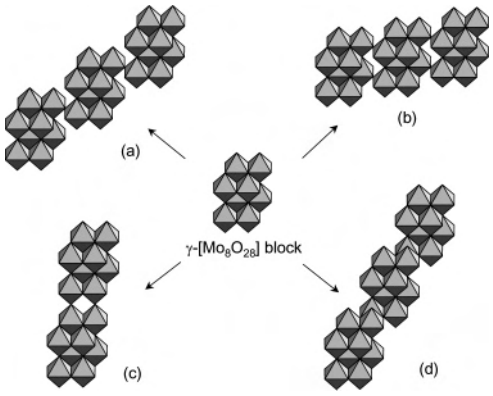

Figure 5. Condensation of γ-$[Mo_8O_{28}]$ subunit formation of the $^1/_\infty[Mo_8O_{27}]^{6-}$ chains (a) in **3**−**5** and the three different $^1/_\infty[Mo_8O_{26}]^{4-}$ chains (b) in **6**, (c) in $(Me{-}NC_5H_5)_4[Mo_8O_{26}]$,[49] and (d) in $(NH_4)_4[Mo_8O_{26}]$.[41]

$$8(\mathbf{1}) + 20H^+ \rightarrow 7(\mathbf{6}) + 10H_2DABCO^{2+} + 14H_2O \quad (13)$$

$$8(\mathbf{2}) + 4H^+ + 2H_2O \rightarrow 3(\mathbf{6}) + 2H_2DABCO^{2+} \quad (14)$$

$$7(\mathbf{3}) + 14H^+ \rightarrow 7(\mathbf{6}) + 14NH_4^+ + 7H_2O \quad (15)$$

Most of the hybrid organic−inorganic compounds based on octamolybdate clusters are built from discrete $[Mo_8O_{26}]^{4-}$ entities. This cluster is reported to be the predominant Mo anion in an aqueous solution of pH values ranging from 2 to 3.5.[53] In the solid state, it has been characterized into nine isomers, namely, α,[57,58] β,[59−61] γ,[62−64] δ,[65−67] ϵ,[68] ξ,[69,70] ξ,[71] η,[72] and θ,[73,74] showing the flexibility of octamolybdate, whose geometry depends strongly on the nature of the organic countercation. In addition, few compounds containing infinite $^1/_\infty[Mo_8O_{26}]^{4-}$ chains have been characterized, and these can be classified into three types depending on the connection mode of the γ-$[Mo_8O_{28}]$ subunits, as shown in Figure 5. The role of the organic cation in the condensation of the octamolybdate subunit, and so the final topology of infinite $^1/_\infty[Mo_8O_{26}]^{4-}$ chains, is nowadays unknown.

(d) $^1/_\infty[Mo_3O_{10}]^{2-}$ Blocks. Compound **2** (2.33,4) is obtained quantitatively from $[Mo_7O_{24}]^{6-}$ as in eq 16 using hydrothermal conditions at 130 °C. Attempts to isolate **2** from $[Mo_7O_{24}]^{6-}$ in ambient conditions were unsuccessful and led systematically to a mixture of **1** and **3**. Because all compounds containing the polymeric $^1/_\infty[Mo_3O_{10}]^{2-}$ chain are reported in the literature, the hydrothermal conditions are necessary to stabilize the $^1/_\infty[Mo_3O_{10}]^{2-}$ chains with H_2DABCO^{2+} as countercations. **2** has been systematically obtained hydrothermally at pH 4 from slurries of **1** (eq 17), **3** (eq 18), and **6** (eq 19) in an aqueous solution.

$$3[Mo_7O_{24}]^{6-} + 7DABCO + 18H^+ + 5H_2O \rightarrow 7(\mathbf{2}) \quad (16)$$

$$3(\mathbf{1}) \rightarrow 7(\mathbf{2}) + 2DABCO + 7H_2O \quad (17)$$

$$3(\mathbf{3}) + 2DABCO + 6H^+ \rightarrow 8(\mathbf{2}) + 6NH_4^+ + 5H_2O \quad (18)$$

$$3(\mathbf{6}) + 2DABCO \rightarrow 8(\mathbf{2}) + 2H_2O \quad (19)$$

Optical Properties. (a) Absorption Threshold and Photochromic Behavior. The optical gaps of the aforementioned compounds, determined in their ground state, i.e., before UV−vis irradiation, were calculated at 3.4, 3.5, 3.1, 3.1, 3.1, and 3.0 eV for **1**−**6**, respectively, which agrees well with the observed hues. These absorption thresholds are assigned to an intramolecular "oxygen to molybdenum charge transfer", whose position differs in energy according to the chemical composition and the structural arrangement of the mineral framework.

Compounds **1**−**5** show photochromic responses under UV excitation [at 254 nm (4.9 eV) or 365 nm (3.4 eV)], as reported in Table 5. Notice that, for irradiation durations of less than 1 h, the coloration disappears after 1 night for **3**, after more than 3 days for **4** and **5**, and after at least 1 week for **1** and **2**, when compounds are kept in darkness in ambient conditions. A moderate heating at about 40 °C may also activate a return to the colorless state. At the opposite, **6** is not photochromic at all, even after excitation for periods as long as $^1/_2$ day.

Compound **1** shows a pale-pink coloration after irradiation at 365 nm and darkens with time. During the first 40 min of the experimental conditions, no color change is visible to the naked eyes, even if reflectivity measurements evidence that the photochromic process has been initiated (Figure 6). Namely, a broadband peak at about 496 nm (2.5 eV) rises up, with an irradiation duration up to a maximum reached after at least 400 min of illumination. Concomitantly, a red shift of the absorption optical gap is observed.

Compound **2** presents a light-reddish-brown coloration under UV excitation and darkens with the irradiation duration. Notice that, under 365 nm excitation, only a slight change in the color is observed with very slow kinetics. In contrast, under 254 nm excitation, the color change is faster and much more intense. This stems from the high optical gap of **2**, which requests excitation at high energy to trigger photochromic reaction via promotion of an electron from the valence band toward the conduction band (vide infra). The evolution of the optical properties of **2**, under illumination at 254 nm only, is displayed in Figure 7. As for **1**, the absorption threshold is progressively red-shifted, while a band around 477 nm (2.6 eV) shows up and gains in intensity. The absorption of **2** covers almost the whole visible spectrum and increases in intensity from long wavelength to short wavelength, which explains the successive white, yellow-brown, and reddish-brown colors. The color change is detected by human eyes only after 30 min of irradiation, and the photoinduced color does not evolve anymore after approximately 430 min.

Compounds **3**−**5** present similar photochromic behaviors, as displayed in Figure 8. All of them become purple under irradiation at 365 and 254 nm, but the kinetics of the color change is much faster when excitation occurs at long wavelength in contrast to **2**. This is probably related to a higher cross section of the $O^{2-} \rightarrow Mo^{6+}$ transition at low energy than at high energy. The purple coloration agrees well with the appearance of a broad absorption band centered around 517 nm (2.4 eV), which might be decomposed in several contributions. As observed previously for **2**, a red shift

(53) Cruywagen, J. J.; Draaijer, A. G.; Heyns, J. B. B.; Rohwer, E. A. *Inorg. Chim. Acta* **2002**, *331*, 322−329.
(54) Lj, I.; Van Hooijdonk, G.; Oosterhout, S.; Kegel, W. K. *Langmuir* **2004**, *20*, 3435−3440.
(55) Howarth, O.; Kelly, P.; Petterson, L. *J. Chem. Soc., Dalton Trans.* **1990**, 81−84.
(56) Isobe, M.; Marumo, F.; Yamase, T.; Ikawa, T. *Acta Crystallogr.* **1978**, *B34*, 2728−2731.
(57) Hagrman, D.; Hagrman, P.; Zubieta, C. *Inorg. Chim. Acta* **2000**, *300*−*302*, 212−224.
(58) Kalpana, G.; Vidyasagar, K. *Acta Crystallogr.* **2005**, *E61*, m1885−m1886.
(59) Muller, E. A.; Narducci Sarjeant, A.; Norquist, A. J. *Acta Crystallogr.* **2005**, *E61*, m730−m732.
(60) Gili, P.; Nunez, P.; Martin-Zarza, P.; Lorenzo-Luis, P. A. *Acta Crystallogr.* **2000**, *C56*, e441−e442.
(61) Li, Q.; Zhang, S.-W. *Z. Anorg. Allg. Chem.* **2005**, *631*, 645−648.
(62) Niven, M. L.; Cruywagen, J. J.; Heyns, J. B. B. *J. Chem. Soc., Dalton Trans.* **1991**, *8*, 2007−2011.
(63) Rarig, R. S., Jr.; Zubieta, J. *Polyedron* **2003**, *22*, 177−188.
(64) Cui, X.-B.; Lu, K.; Fan, Y.; Xu, J.-Q.; Ye, L.; Sun, Y.-H.; Li, Y.; Yu, H.-H.; Yi, Z.-H. *J. Mol. Struct.* **2005**, *743*, 151−155.
(65) Xi, R.; Wang, B.; Isobe, K.; Nishioka, T.; Toriumi, K.; Ozama, Y. *Inorg. Chem.* **1994**, *33*, 833−836.
(66) Rarig, R. S., Jr.; Zubieta, J. *Inorg. Chim. Acta* **2001**, *312*, 188−196.
(67) Burkholder, E.; Zubieta, J. *Inorg. Chim. Acta* **2005**, *358*, 116−122.
(68) Hagrman, D.; Zubieta, C.; Rose, D. J.; Zubieta, J.; Haushalter, R. C. *Angew. Chem., Int. Ed. Engl.* **1997**, *36*, 873−876.
(69) Burkholder, E.; Zubieta, J. *Solid State Sci.* **2004**, *6*, 1421−1428.
(70) Allis, D. G.; Rarig, R. S.; Burkholder, E.; Zubieta, J. *J. Mol. Struct.* **2004**, *688*, 11−31.
(71) Xu, J.-Q.; Wang, R.-Z.; Yang, G.-Y.; Xing, Y.-H.; Li, D.-M.; Bu, W.-M.; Ye, L.; Fan, Y.-G.; Yang, G.-D.; Xing, Y.; Lin, Y.-H.; Jia, H.-Q. *Chem. Commun.* **1999**, 983−984.
(72) Rarig, R. S.; Bewley, L.; Burkholder, E.; Zubieta, J. *Indian J. Chem.* **2003**, *42A*, 2235−2243.
(73) Allis, D. G.; Burkholder, E.; Zubieta, J. *Polyhedron* **2004**, *23*, 1145−1152.
(74) Xiao, D.; Hou, Y.; Wang, E.; Wang, S.; Li, Xu, Y. L.; Changwen, H. *Inorg. Chim. Acta* **2004**, *357*, 2525−2531.

Table 5. Optical Characteristic of Compounds **1**−**6**

compound	*a*	*b*	*c*	*d*	*e*	*f*
1	365 (3.4)	365 (3.4)	white	pink	496 (2.5)	>400
2	254 (4.9)	352 (3.5)	white	brown	477 (2.6)	430
3	365 (3.4)	400 (3.1)	pale yellow	purple	517 (2.4)	360
4	365 (3.4)	400 (3.1)	yellowish white	purple	517 (2.4)	210
5	365 (3.4)	400 (3.1)	yellowish white	purple	517 (2.4)	210
6	365 (3.4) or 254 (4.9)	413 (3.0)	pale yellow	pale yellow		

[a] UV excitation [nm (eV)]. [b] Optical gap (eV) in the stable state. [c] Color before irradiation. [d] Color after irradiation. [e] Photoinduced absorption band energy [nm (eV)]. [f] Duration for which no color evolution is observed under UV excitation (min).

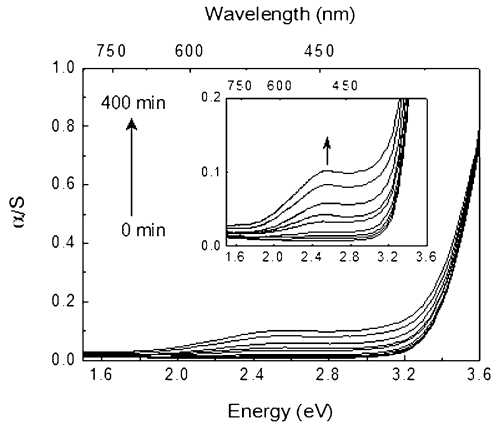

Figure 6. Evolution of the Kubelka−Munk transformed reflectivity of **1** vs energy (eV) for different irradiation durations at 365 nm (0, 10, 30, 60, 120, 180, 240, 330, and 400 min). The inset refers to an enlargement of the general plot, which highlights the increase of the photogenerated absorption band with irradiation.

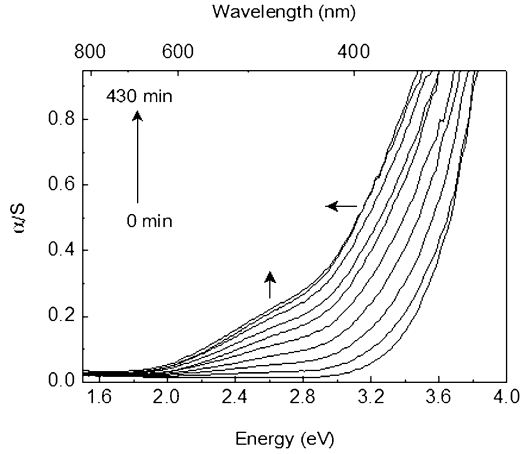

Figure 7. Evolution of the Kubelka−Munk transformed reflectivity of **2** vs energy for different irradiation durations at 254 nm (0, 20, 50, 90, 150, 210, 270, 330, 360, and 430 min).

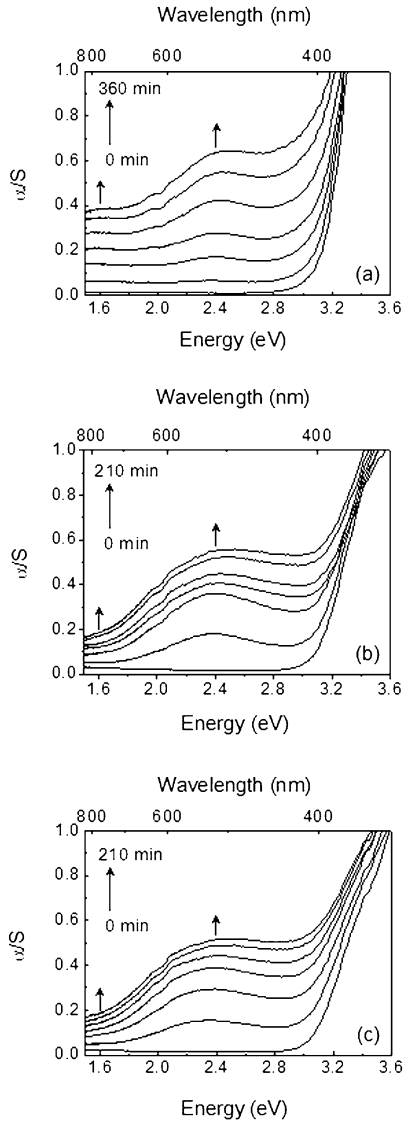

Figure 8. Kubelka−Munk transformed reflectivity of **3** (a), **4** (b), and **5** (c) vs energy after irradiation at 365 nm for different durations (0, 10, 30, 60, 120, 240, and 360 min for **3** and 0, 10, 30, 60, 90, 150, and 210 min for **4** and **5**).

of the absorption spectrum occurs with the illumination duration. In addition, in contrast to **1** and **2**, an absorption band in the IR region around 775 nm (1.6 eV) rises up with exposure. This band reaches its maximum after 360 min for **3** and 210 min for **4** and **5**, similar to the absorption band at 517 nm (2.4 eV).

(b) Origin of the Photochromism. The photochromism in organic−inorganic hybrid materials based on polyoxometalates is commonly explained in terms of Yamase's model,[75] which speculates that electrons of O_t atoms (the strongest Mo-bonded O atom with σ- and π-bonding interactions) are promoted to the Mo^{6+} 4d block under UV−vis excitation and trapped in a metastable state with the appearance of Mo^V. Formally, the photogenerated hole at the top of the O 2p block is annihilated afterward because of the displacement of a labile proton of the N atom of the organoammonium countercation toward a bridged O atom (e.g., μ_2- or μ_3-O) at the photoreduced Mo site and to the consecutive donation of the nonbonding electrons of the amino N atom to the O_t atom with the formation of a "charge-transfer complex". The Mo^V cations with a d^1 electronic configuration may then be involved in d−d transitions and intervalence $Mo^V + Mo^{VI} \rightarrow Mo^{VI} + Mo^V$ charge transfer inducing new colors. Formally, the organic cations play a key role in the stabilization of the photoinduced metastable state coloration

(75) Yamase, T. *Chem. Rev.* **1998**, *98*, 307−325.

because the oxidized state of the organic cation must be sufficiently stable to avoid the return to the ground state and bleaching. Consequently, it turns out that three main factors may affect the photochromic response of such hybrid materials: the chemical nature of the inorganic components and its organic counterpart, and the organic−inorganic interface, i.e., the hydrogen-bond subnetwork.

(i) Influence of the Inorganic Component. Compound **1** becomes pink under UV irradiation as $[^{i}PrNH_3]_6[Mo_7O_{24}]\cdot 3H_2O$,[27] $[PrNH_3]_6[Mo_7O_{24}]\cdot 3H_2O$,[25] and $(C_6H_{18}N_2)_3[Mo_7O_{24}]\cdot 4H_2O$.[37] For the latter, the coloration is described in the literature as reddish brown by the authors, although the reflectivity curve evidences the same features as those of **1**, suggesting that the four materials display the same color in their photogenerated state. In the same way, compounds **3**−**5**, which contain the same mineral framework, become all-purple after irradiation, while compound **2** shifts to reddish-brown in its excited state like the recently reported zigzag $^1/_\infty[Mo_3O_{10}]^{2-}$ chain containing $(C_6H_{18}N_2)[Mo_3O_{10}]$.[36] At first sight, these observations infer that a hybrid material with a given inorganic block displays a well-defined hue in its photoinduced state, whatever the chemical nature of the organic countercation.

(ii) Influence of the Organic Countercations. Apart from the nature of the inorganic block, the organic component may strongly influence the photochromic response (e.g., the kinetics of the color change) of the hybrid materials, as displayed by a comparison of the optical curves of compounds **3**−**5**. In these materials, the photochromic response may be interpreted, in a first approximation, as the sum of two distinct photochromic processes associated to lattices 1 and 2, respectively (see Figure 4). Both compounds **3** and **4** contain H_2DABCO^{2+} cations in lattice 1, while NH_4^+ and H_2pipz^{2+} cations occupy lattice 2, respectively. Because only NH_4^+-containing molybdate salts [e.g., $(NH_4)_6[Mo_7O_{24}]\cdot 4H_2O$[75]] are reported to be not photochromic, we may reasonably attribute the origin of the photochromic change in **3** to the presence of H_2DABCO^{2+} cations in lattice 1. A similar photochromic process is expected to occur in **4**, with hydrogen transfer of the H_2DABCO^{2+} cations to the μ^2-O_{12} and/or μ^3-O_7 of the $^1/_\infty[Mo_8O_{27}]^{6-}$ cluster, but this time the photochromic response is enhanced thanks to hydrogen transfer from H_2pipz^{2+} cations toward the O_t atoms O_9 and O_{14} of the mineral chains occurring in lattice 2. At first sight, the faster coloration kinetics of **4** compared to **3** (rigorously observed in the same experimental conditions) might be explained based on the higher ability of H_2pipz^{2+} cations compared to NH_4^+ cations to retrocede one hydrogen to the mineral framework (leading to a higher concentration of reduced Mo^{5+} cations in the photogenerated state). Moreover, **4** and **5** contain both H_2pipz^{2+} cations in lattice 2 and differ only by the presence of H_2DABCO^{2+} or H_2pipz^{2+} in lattice 1. However, their optical behaviors are very similar, which suggests that their overall photochromic responses are mainly dependent on the photochromic process involving H_2pipz^{2+} cations in lattice 2.

(iii) Interaction between the Mineral Blocks and the Organic Cations. As shown previously, the presence of an appropriate hydrogen-bonding network between both organic and inorganic components is essential to inducing photochromism. For example, the structure of **6** shows that the H_2DABCO^{2+} entities do not interact directly via hydrogen bonds with the $^1/_\infty[Mo_8O_{26}]^{4-}$ clusters but interact only indirectly via the water molecules present in the network, which may explain why no modifications of the optical properties of this material are observed under UV irradiation.

Conclusion

The study of the hybrid organic−inorganic materials based on molybdate, DABCO, and pipz clearly evidences that both the pH and DABCO/$[Mo_7O_{24}]^{6-}$ concentration ratio strongly influence the nature of the mineral species stabilized in the solid state. A rational design of the synthesized hybrid organic−inorganic materials has been proposed in terms of these two parameters, opening up the possibility for better control of the synthetic conditions to prepare new materials. Moreover, the optical properties of **1**−**5** under illumination highlight the importance of accounting for the organic−inorganic interface and the nature of the two components for the generation of new photochromic properties.

Supporting Information Available: X-ray crystallographic data in CIF format and atomic coordinates, isotropic and anisotropic displacement parameters, and main distances for **1** and **2**. This material is available free of charge via the Internet at http://pubs.acs.org.

IC0621502